nature communications

Article

https://doi.org/10.1038/s41467-025-60423-y

Mechanisms of aureobasidin A inhibition and drug resistance in a fungal IPC synthase complex

Received: 3 October 2024

Accepted: 22 May 2025

Published online: 30 May 2025

Check for updates

Xinyue Wu[1,2], Xin Gong[1,2,3] ✉ & Tian Xie[1,2] ✉

The enzyme inositol phosphorylceramide (IPC) synthase is essential for survival and virulence in fungi, while absent in mammals, thus representing a potential target for antifungal treatments. Aureobasidin A (AbA), a natural cyclic peptide, displays antifungal activity and inhibits IPC synthase, but the precise molecular mechanism remains unclear. Here, we present the cryo-EM structure of the *Saccharomyces cerevisiae* IPC synthase, composed of catalytic subunit Aur1 and regulatory subunit Kei1, in its AbA-bound state. The complex is resolved as a dimer of Aur1-Kei1 heterodimers, with Aur1 mediating homodimerization. AbA occupies a predominantly hydrophobic pocket in the catalytic core domain of each Aur1 subunit, blocking the entry of both substrates. Mutations conferring AbA resistance cluster near the AbA-binding site, thus interfering with AbA binding. Our study lays a foundation for the development of therapeutic drugs targeting fungal IPC synthase.

Fungal pathogens are accountable for a wide range of human diseases, including superficial infections, mucosal infections, allergic infections, and severe chronic as well as acute invasive infections[1–4]. Annually, fungal infections impact over a billion individuals and contribute to more than 1.6 million fatalities, posing a substantial global health concern[5,6]. Despite the widespread occurrence of fungal diseases, there has been a dearth of research on the biology of fungal pathogens and their virulence, impeding the progress in developing innovative antifungal drugs[7,8]. Presently, only three primary classes of clinical drugs—polyenes, echinocandins, and azoles—are accessible for treating fungal ailments[9,10]. However, these medications encounter challenges such as host toxicity, suboptimal pharmacokinetics, or limited antifungal coverage[10]. Furthermore, fungi have been evolving rapidly, leading to the constant emergence of antifungal drug resistance and subsequent treatment failures[11–16]. Hence, it is crucial to identify alternative therapeutic targets for combating fungal infections.

Pathogenic fungi possess distinctive sphingolipids, such as inositol phosphorylceramides (IPCs) and their mannosylated derivatives, which are critical for fungal survival and virulence, yet are absent in human hosts[17–21]. Disruption the levels of IPCs and their derivatives leads to impaired fungal growth[22]. The synthesis of IPCs is catalyzed by an enzyme known as IPC synthase, which facilitates the transfer of a phosphorylinositol head group from the donor substrate phosphatidylinositol (PI) to the acceptor substrate ceramide[23] (Fig. 1A). Given that IPC synthase does not exist in mammals, it presents a highly attractive target for therapeutic intervention against fungal infections[24,25]. Additionally, IPC synthase has been identified in protozoan pathogens, establishing it as a promising target for the development of anti-protozoal drugs[26–29].

Aureobasidin A (AbA) is a natural cyclic depsipeptide antifungal antibiotic isolated from the fungus *Aureobasidium pullulans*, known for its potent activity against a wide range of pathogenic fungi[30,31] (Fig. 1B). In animal models, AbA has demonstrated superior efficacy against many fungal pathogens compared to traditional antifungal drugs like fluconazole and amphotericin B[30]. AbA has been shown to inhibit the fungal IPC synthase at concentrations as low as the subnanomolar level[22]. Previous studies have explored the structure-activity relationships (SAR) of AbA by modifying it to create various

[1]Shenzhen Key Laboratory of Plant Genetic Engineering and Molecular Design, Department of Biology, School of Life Sciences, Southern University of Science and Technology, Shenzhen, Guangdong 518055, China. [2]Department of Chemical Biology, School of Life Sciences, Southern University of Science and Technology, Shenzhen, Guangdong 518055, China. [3]Institute for Biological Electron Microscopy, Southern University of Science and Technology, Shenzhen, Guangdong 518055, China. ✉e-mail: gongx@sustech.edu.cn; xiet@mail.sustech.edu.cn

https://doi.org/10.1038/s41467-025-60423-y

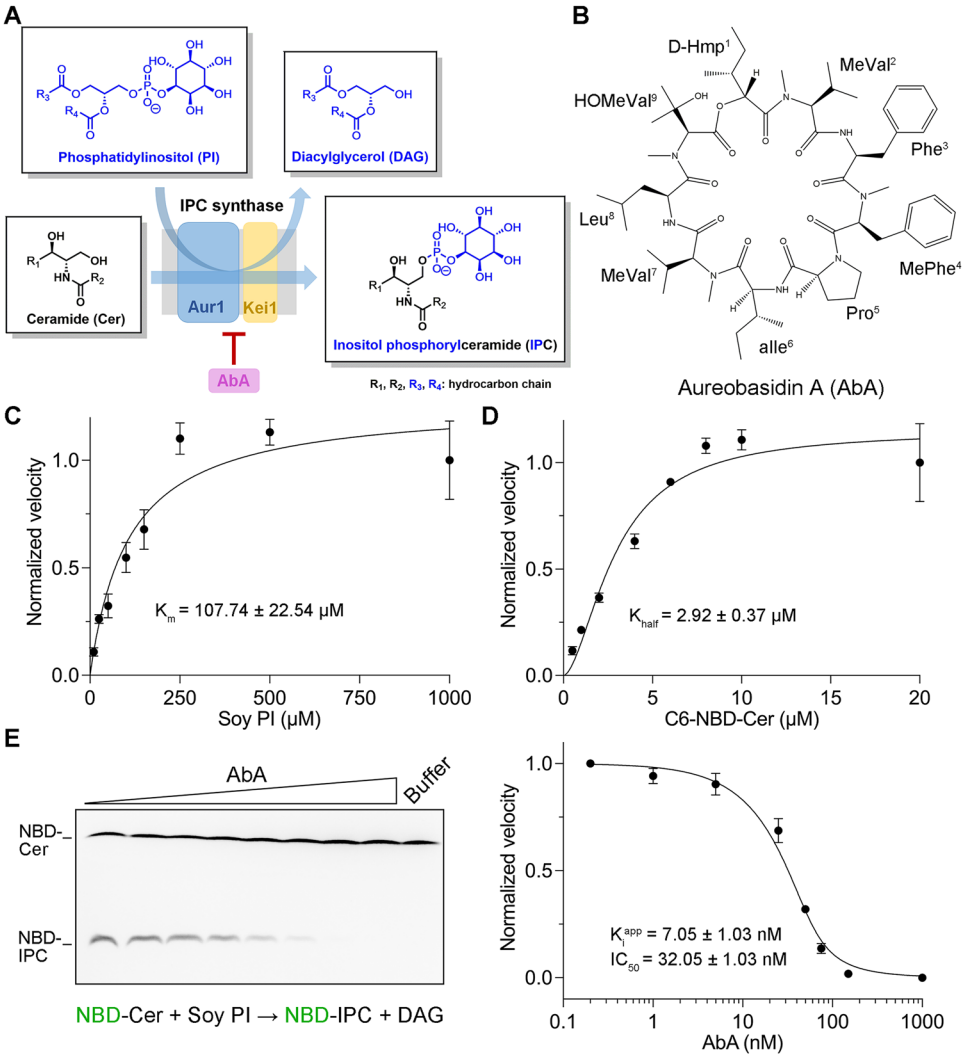

Fig. 1 | Functional characterization of the *S. cerevisiae* IPC synthase complex. **A** The *S. cerevisiae* IPC synthase, composed of Aur1 and Kei, catalyzes the formation of inositol phosphorylceramide (IPC) by transferring a phosphorylinositol head group from phosphatidylinositol (PI) to ceramide. The activity of IPC synthase can be inhibited by the specific inhibitor aureobasidin A (AbA). **B** Chemical structure of the cyclic depsipeptide inhibitor AbA. **C** Normalized IPC synthase activity versus PI concentration for the Aur1-Kei1 complex. The activity curve follows the Michaelis-Menten equation. Each data point represents the mean ± SD of three independent experiments. **D** Normalized IPC synthase activity versus ceramide concentration for the Aur1-Kei1 complex. The activity curve exhibits an allosteric sigmoidal behavior. Each data point represents the mean ± SD of three independent experiments. **E** AbA inhibits the in vitro activity of IPC synthase in a dose-dependent manner. Left: a representative result of thin-layer chromatography (TLC). Right: quantification and statistical analysis of three independent TLC results. Each data point represents the mean ± SD of three independent experiments. Source data are provided as a Source Data file.

derivatives[32,33]. However, a deeper understanding of the mechanism by which AbA acts on IPC synthase will significantly accelerate its further optimization.

The generation of dominant *Saccharomyces cerevisiae* (*S. cerevisiae*) mutants resistant to AbA led to the identification of its direct target, named *AUR1*, for aureobasidin resistance[34,35]. The *AUR1* gene, also known as *IPC1*, encodes the catalytic subunit Aur1 of IPC synthase. The *S. cerevisiae* Aur1 (*Sc*Aur1) is a 401-residue (~45 kDa) membrane-embedded protein situated in the Golgi apparatus, featuring an active site that includes a conserved catalytic triad composed of two histidine residues (His255, His294) and one aspartic acid residue (Asp298)[36,37]. Mutation of His294 to alanine has been shown to impair enzyme activity and yeast growth[36]. Fungal Aur1 homologs share approximately 60% sequence similarity, and their catalytic triad closely resembles that of animal sphingomyelin synthase (SMS)[38]. In addition to the catalytic subunit Aur1, a 221-residue (~25 kDa) regulatory subunit named Kei1 was identified as an essential component of the IPC synthase complex in *S. cerevisiae*[39]. Kei1 is crucial for both the enzymatic activity and Golgi localization of the IPC synthase complex and exhibits about 40% sequence similarity among fungal Kei homologs[39]. However, the lack of a resolved structure for the IPC synthase complex has limited our understanding of the precise functional roles of the Aur1 and Kei1 subunits within the complex and constrained our ability to rationalize drug-resistance mechanisms of the mutations.

In this study, we determined a high-resolution structure of the *S. cerevisiae* Aur1-Kei1 complex bound to AbA. Structural analysis suggests that AbA inhibits IPC synthase by blocking the entry of both substrates. Notably, AbA-resistant mutations cluster around the AbA-binding site, indicating that these mutations confer resistance by directly disrupting AbA binding, as supported by biochemical binding assays. These findings advance our understanding of the inhibitory mechanism of AbA on IPC synthase and the emergence of AbA-resistant mutants, providing a valuable template for developing antifungal drugs targeting IPC synthase.

Results

In vitro functional characterization of the *S. cerevisiae* IPC synthase complex

First, we attempted to express and purify the *S. cerevisiae* Aur1-Kei1 complex, as well as the Aur1 and Kei1 subunits individually (see Methods for detail). Size-exclusion chromatography (SEC) analysis revealed that the Aur1-Kei1 complex exhibited good solution behavior, whereas Aur1 alone did not, suggesting that Kei1 is necessary for the proper folding of Aur1 (Fig. S1A). Kei1 alone eluted in SEC with a peak position similar to that of the Aur1-Kei1 complex, and native-PAGE analysis further indicated that Kei1 may exist in various oligomeric states in solution (Fig. S1A, B). To clarify the multiple bands observed in the SDS-PAGE gel of the Aur1-Kei1 complex, we performed deglycosylation, affinity-tag cleavage, and Western blotting analyses (Fig. S1C–E). The results suggest that the two major bands of Aur1 likely correspond to the glycosylated and non-glycosylated forms, while the two major bands of Kei1 likely correspond to the Flag-tagged and tag-degraded forms, respectively (Fig. S1C–E).

To characterize the function of the purified IPC synthase, we utilized an in vitro fluorescence-based activity assay with an NBD-labelled ceramide substrate, as previously described[36,40,41]. The IPC synthase activity was assessed by detecting and quantifying the produced fluorescent NBD-IPC bands on thin-layer chromatography (TLC) plates. The activity of the wild-type (WT) Aur1-Kei1 complex was promptly detected (Fig. S2A). As a negative control, the catalytic mutant of Aur1 (H255A) abolished IPC synthase activity (Fig. S2B). The WT Aur1-Kei1 complex was also effectively inhibited by the AbA inhibitor (Fig. S2B), further confirming the proper function of the purified complex. In contrast, no enzymatic activity was detected for neither the Aur1 nor Kei1 subunit alone (Fig. S2C), indicating that the Kei1 is not only essential for the proper folding of Aur1 but also critical for the enzymatic activity of the IPC synthase complex.

To study the enzymatic kinetics of the purified IPC synthase complex, we measured its activity in the presence of varying concentrations of PI or ceramide (Fig. S2D, E). The activity curve of IPC synthase with different PI concentrations follows the Michaelis-Menten equation, yielding a K_m value of ~108 μM for PI (Fig. 1C). In contrast, the activity curve with varying ceramide concentrations fits an allosteric sigmoidal equation, with a K_{half} value of ~3 μM for ceramide (Fig. 1D). These kinetic values are within the same order of magnitude as those reported for unpurified membrane-embedded IPC synthase, which were 555 μM and 3 μM, respectively[42]. The IPC synthase activity was effectively inhibited by AbA, with a half-maximal inhibitory concentration (IC_{50}) and an apparent K_i (K_i^{app}) of ~32 nM and ~7 nM, respectively, as calculated using the Morrison equation in the presence of 50 nM Aur1-Kei1 complex, 500 μM soy PI, and 10 μM ceramide (Fig. 1E).

Structural determination of the AbA-bound IPC synthase complex

Next, we subjected the purified Aur1-Kei1 complex to single-particle cryo-EM analysis, which revealed the existence of two distinct particle classes with different sizes (Fig. S3A). The AlphaFold-Multimer[43,44]-predicted structural model of the Aur1-Kei1 heterodimer fits well with the smaller particle class, while a dimer of predicted Aur1-Kei1 heterodimer aligns well with the larger particle class (Fig. S3A). Consistent with this, SEC, cross-linking, and native-PAGE analyses showed that the IPC synthase complex exists as a mixture of 1:1 Aur1-Kei1 and 2:2 Aur1-Kei1 complexes in solution (Fig. S3B, C). The former SEC peak (peak 1) contains a mixture of 1:1 and 2:2 complexes, while the later SEC peak (peak 2) primarily contains the 1:1 complex (Fig. S3C). We then conducted activity assays of the IPC synthase from both SEC peaks, revealing that the IPC synthase from both peaks exhibited nearly identical enzymatic activity and could be inhibited by AbA to the same extent (Fig. S3D). These results suggest that dimerization of the IPC synthase complex does not affect its enzymatic activity or its inhibition by AbA. However, the physiological role of IPC synthase complex dimerization in vivo remains to be further explored.

Our initial attempts to determine the structure of the Aur1-Kei1 complex were conducted using the apo Aur1-Kei1 complex without any added substrates or inhibitors (Fig. S3A). However, cryo-EM analysis of the apo complex revealed 2D classes with relatively poor features (Fig. S3A), preventing us from resolving its high-resolution 3D structure. We speculated that the apo Aur1-Kei1 complex might exhibit high conformational flexibility, rendering it unstable for high-resolution structural determination. We then attempted to determine the structure of the Aur1-Kei1 complex in the presence of PI or ceramide substrate, but these efforts were also unsuccessful. Finally, we conducted cryo-EM analysis on the Aur1-Kei1 complex incubated with AbA (Fig. S4A). Similar to the apo complex, both 1:1 and 2:2 Aur1-Kei1 complexes were observed in the cryo-EM images (Fig. S4A). The relatively small molecular size of the 1:1 Aur1-Kei1 complex (~70 kDa), which lacks distinguishable soluble regions, continued to hinder structural determination. However, the larger 2:2 Aur1-Kei1 complex allowed for successful 3D reconstruction, resulting in a map with an overall resolution of 3.17 Å (Fig. S4B-E, Table S1). We speculated that the AbA inhibitor improved the conformational stability of the complex, thereby enabling high-resolution structural determination.

Supporting our speculation regarding the stability of the Aur1-Kei1 complex in the presence of substrates or the AbA inhibitor, thermal shift assays (TSA), a widely used method for assessing protein stability in structural and functional studies[45–48], revealed that incubation with PI or ceramide did not enhance protein stability compared to the control (Fig. S5A, B). In contrast, incubation with the AbA inhibitor significantly increased the melting temperature (T_m) of the Aur1-Kei1 complex by nearly 10 °C (Fig. S5A, B).

Architecture of the IPC synthase complex

The high-quality density map of the 2:2 Aur1-Kei1 complex allowed for the construction of an atomic model, with most residues clearly resolved (Fig. S6A, B). The N- and C-termini of Aur1 (residues 1–15 and 351–401, respectively) and two short internal loops of Kei1 (residues 112–135 and 188–197, respectively) were not resolved, likely due to their intrinsic flexibility. The 2:2 Aur1-Kei1 complex exists as a dimer of Aur1-Kei1 heterodimers, with two catalytic subunits of Aur1 centrally located and regulatory subunit Kei1 positioned at each end (Fig. 2). To the best of our knowledge, this represents the first structure reported for the fungal IPC synthase family.

Each Aur1 subunit consists of eight transmembrane helices (TM1-TM8), with both the N- and C-termini facing the cytosol (Figs. 2, 3A). Among these, TM3-TM8 form a catalytic cavity, with the catalytic triad (His255, His294, Asp298) centrally positioned within the cavity near the luminal surface of the transmembrane region (Fig. 3A–C). Thus, we refer to TM3-TM8 as the catalytic core domain of Aur1. In contrast, TM1-TM2 are folded away from the catalytic cavity, and we designate this region as the N-terminal domain (NTD) of Aur1 (Figs. 2, 3A, B). In addition to the eight TMs, the Aur1 structure includes six short helices: one cytosolic helix (CH1) preceding TM1, two luminal helices (LH1 and LH2) between TM3 and TM4, and three luminal helices (LH3–LH5) between TM5 and TM6 (Figs. 2, 3A). The dimerization of Aur1 is primarily mediated by extensive hydrophobic interactions between the TM1 and CH1 helices of the two Aur1 protomers (Fig. 3D). In addition to the protein-mediated dimerization interface, several lipid or lipid-like densities were observed at the interface of the Aur1 homodimer (Fig. S6C, left), which may also contribute to stabilizing the homodimer interface.

The Kei1 subunit consists of four transmembrane helices (TM1-TM4), with both the N- and C-termini also facing the cytosol (Figs. 2, 3A). The heterodimeric interface between Aur1 and Kei1 is located outside the catalytic cavity of Aur1 (Figs. 2, 3B), suggesting that Kei1 is

https://doi.org/10.1038/s41467-025-60423-y

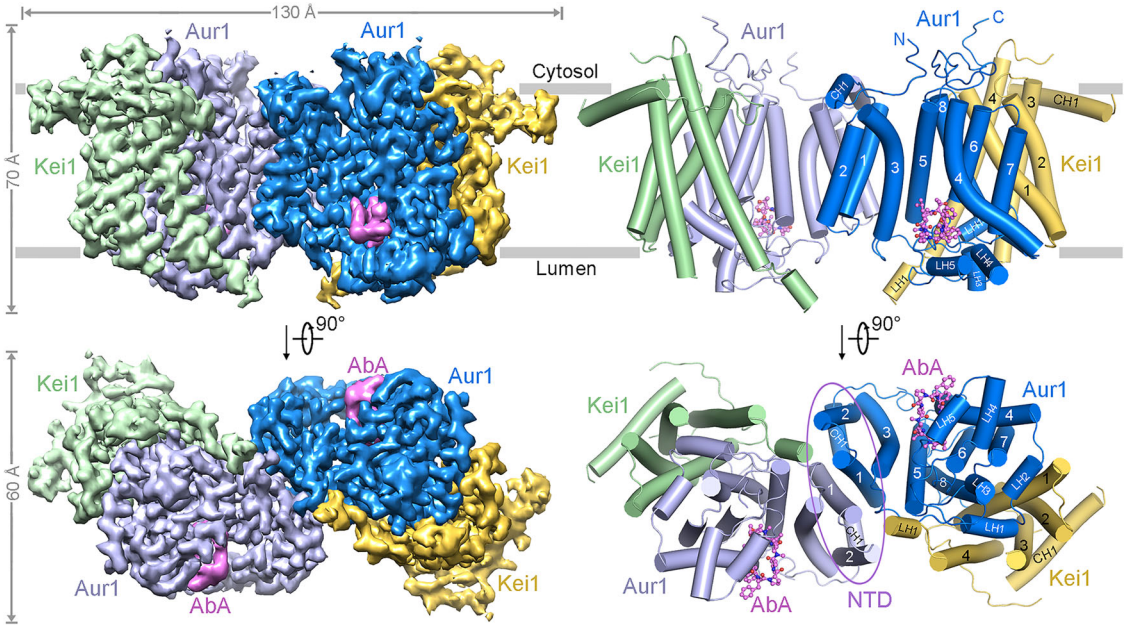

Fig. 2 | Overall structure of the AbA-bound IPC synthase complex. Cryo-EM map (left) and structural model (right) of the AbA-bound Aur1-Kei1 complex. The complex exists as a dimer of Aur1-Kei1 heterodimers, with Aur1 mediating homodimerization. The two Aur1 subunits are colored in marine and light blue, while the two Kei1 subunits are colored in yellow and light green. AbA is depicted in magenta, positioned within the catalytic core domain of the Aur1 subunit. NTD N-terminal domain, LH luminal helix, CH cytosolic helix.

not directly involved in the catalytic reactions of Aur1. The interface between Aur1 and Kei1 is characterized by extensive hydrophobic and hydrophilic interactions (Fig. S7A-E). Lipid or lipid-like densities were also observed at the Aur1-Kei1 heterodimer interface (Fig. S6C, right), which may further stabilize the heterodimer interface. A previously identified F103I mutation in Kei1 was reported to disrupt the interaction between Aur1 and Kei1, thus abolishing the enzymatic activity of the complex in vivo[39]. The Phe103 residue of Kei1 is located in close proximity to the Aur1 subunit (Figs. 3E and S7C), highlighting the importance of the heterodimeric interface between Aur1 and Kei1 for the assembly and activity of the IPC synthase complex.

AbA binding site

Within the catalytic core domain of each Aur1 protomer, a distinct circular density was observed that fits perfectly with the cyclic AbA depsipeptide, with its side chains clearly resolved (Fig. 4A). The AbA molecule is situated in a predominantly hydrophobic pocket formed by the TM3, TM4, and TM6 helices, along with the LH4 and LH5 regions of Aur1 (Fig. 4A, B). Conservation analysis reveals that the residues within the AbA binding pocket are highly conserved across fungi (Figs. 4C, D, and S8), which aligns with the broad antifungal spectrum of AbA.

Numerous hydrophobic residues in Aur1 coordinate the binding of the AbA molecule (Fig. 4D). Among these, Phe158 in Aur1, an important residue for AbA resistance (to be discussed later), packs against Phe^3 in AbA, likely playing a crucial role in orienting the AbA configuration (Fig. 4D). Beyond hydrophobic interactions, the AbA molecule is further stabilized by two potential hydrogen bonds with Aur1: one between the side chain of Tyr102 in Aur1 and the carbonyl group of MeVal^7 in AbA, and another between the side chain of His157 in Aur1 and the hydroxyl group of HOMeVal^9 in AbA (Fig. 4D). His157 in Aur1 is another key residue associated with AbA resistance, which will also be discussed below. Based on the structure, several side chains of AbA, such as MePhe^4 and alle^6, are exposed and extend toward the outside of the AbA-binding pocket (Fig. 4B–D), which may provide space to accommodate structural modifications to AbA for improved specificity or potency—a speculation that requires further validation. The structural insights into AbA-Aur1 binding resolved here could serve as a blueprint for further optimizing AbA derivatives, with the aim of more effectively combating fungal infections.

AbA blocks the entry of both substrates

As mentioned earlier, we were unable to resolve the structures of the Aur1-Kei1 complex bound to PI or ceramide substrate. However, the structures of a human functional homolog of Aur1, sphingomyelin synthase-related protein 1 (SMSr), bound to its substrates, were recently reported[49] (Fig. 5A). Like Aur1, SMSr is a membrane-embedded transferase that catalyzes the transfer of a phosphoethanolamine (PEA) group from phosphatidylethanolamine (PE) to ceramide, thereby generating ceramide phosphoethanolamine (CPE) and diacylglycerol (DAG)[49]. SMSr consists of six transmembrane helices (TM1-TM6), which align well with TM3-TM8 of the catalytic core domain of Aur1 (Fig. 5B). Notably, the highly conserved catalytic triad residues in Aur1 (His255/His294/Asp298) and SMSr (His301/His344/Asp348) are also well-aligned (Figs. 5B and S9A). This structural analysis suggests that, despite utilizing different phospholipids as substrates, Aur1 and SMSr may share similar substrate-binding pockets and catalytic mechanisms for transferring the polar head of phospholipids to ceramide. Although SMSr is a functional homolog of Aur1, AbA shows no inhibitory effect on SMSr (Fig. S9B), highlighting the specificity of AbA towards fungal IPC synthase inhibition.

To evaluate the phospholipid substrate specificity of Aur1 and SMSr, molecular docking analysis[50,51] of Aur1 with the PI substrate was performed to identify the potential PI-binding pocket on Aur1. A PI molecule was docked within the catalytic core domain of Aur1 in the luminal leaflet, with its polar head positioned in close proximity to the catalytic His255 and His294 residues (Fig. S10A). Superimposition of the PI-docked Aur1 structure with the DAG/PEA (hydrolyzed products of the PE substrate)-bound SMSr structure revealed that PI and DAG/PEA occupy roughly similar positions (Fig. S10B). However, the polar inositol phosphate moiety of PI and the polar PEA molecule, which determine the specificity of the phospholipid substrates (PI vs. PE), are located far apart from each other (Fig. S10B). Further structural analysis suggested that the binding sites for the polar heads of PI and PE

https://doi.org/10.1038/s41467-025-60423-y

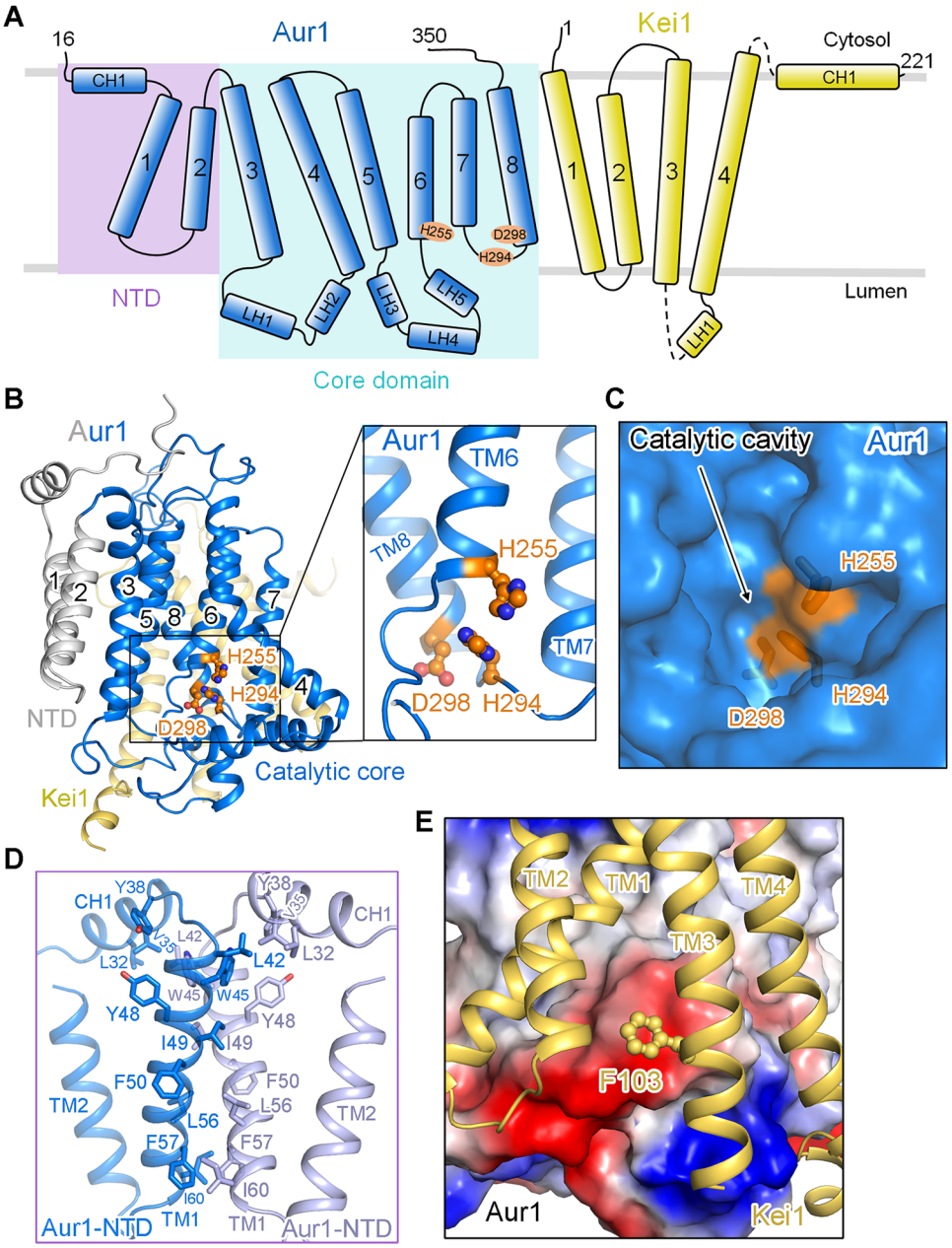

Fig. 3 | Structural analysis of the Aur1-Kei1 complex. A Schematic representation of the topology of Aur1 and Kei1. The Aur1 subunit consists of an NTD and a catalytic core domain, with the catalytic triad residues highlighted in orange. **B** Structural localization of the Aur1 catalytic triad residues. **C** The catalytic cavity within the Aur1 core domain. **D** The homodimerization interface between the two Aur1 protomers. **E** Phe103 of Kei1, previously reported to disrupt interaction with Aur1 when mutated, is located in close proximity to Aur1.

substrates are largely defined by the connection region between TM5 and TM6 in Aur1 and the corresponding region between TM3 and TM4 in SMSr (Fig. S10C). Additional studies are required to confirm the precise PI-binding site on Aur1 and elucidate the mechanisms underlying phospholipid substrate specificity.

In the substrate-bound SMSr structures, both DAG/PEA and ceramide molecules are positioned in close proximity to the catalytic triad residues of SMSr (Fig. 5A). Superimposing the AbA-bound Aur1-structure with the substrate-bound SMSr structures reveals that both lipid substrates of SMSr would clash with the AbA molecule in the AbA-bound Aur1 structure (Fig. 5C, D). Additionally, molecular docking of Aur1 with PI also indicates that the docked PI overlaps with the AbA inhibitor (Fig. S10D). These findings suggest that the AbA-binding pocket in Aur1 likely overlaps with its potential substrate-binding pockets, implying that AbA inhibits the IPC synthase activity of the Aur1-Kei1 complex by blocking the entry of both substrates. Further studies are required to verify the precise substrate-binding sites on Aur1, in order to definitively establish the mechanism of action for AbA.

AbA resistance mechanism

Previous fungal genetic and chemical screens have identified several mutations in Aur1 that confer resistance to AbA, including L137F/H157Y and F158Y in *S. cerevisiae* Aur1 (*Sc*Aur1), G240C in *Schizosaccharomyces pombe* Aur1 (*Sp*Aur1), and G275V in *Aspergillus nidulans* Aur1 (*An*Aur1)[34,35,52,53]. Gly240 in *Sp*Aur1 and Gly275 in *An*Aur1 correspond to Ala240 in *Sc*Aur1. While the Leu137 mutation site is located at the heterodimeric interface between Aur1 and Kei1, far from the AbA-binding pocket, the mutation sites His157, Phe158, and Ala240 cluster around the AbA-binding site (Fig. 6A). This suggests that the AbA-

https://doi.org/10.1038/s41467-025-60423-y

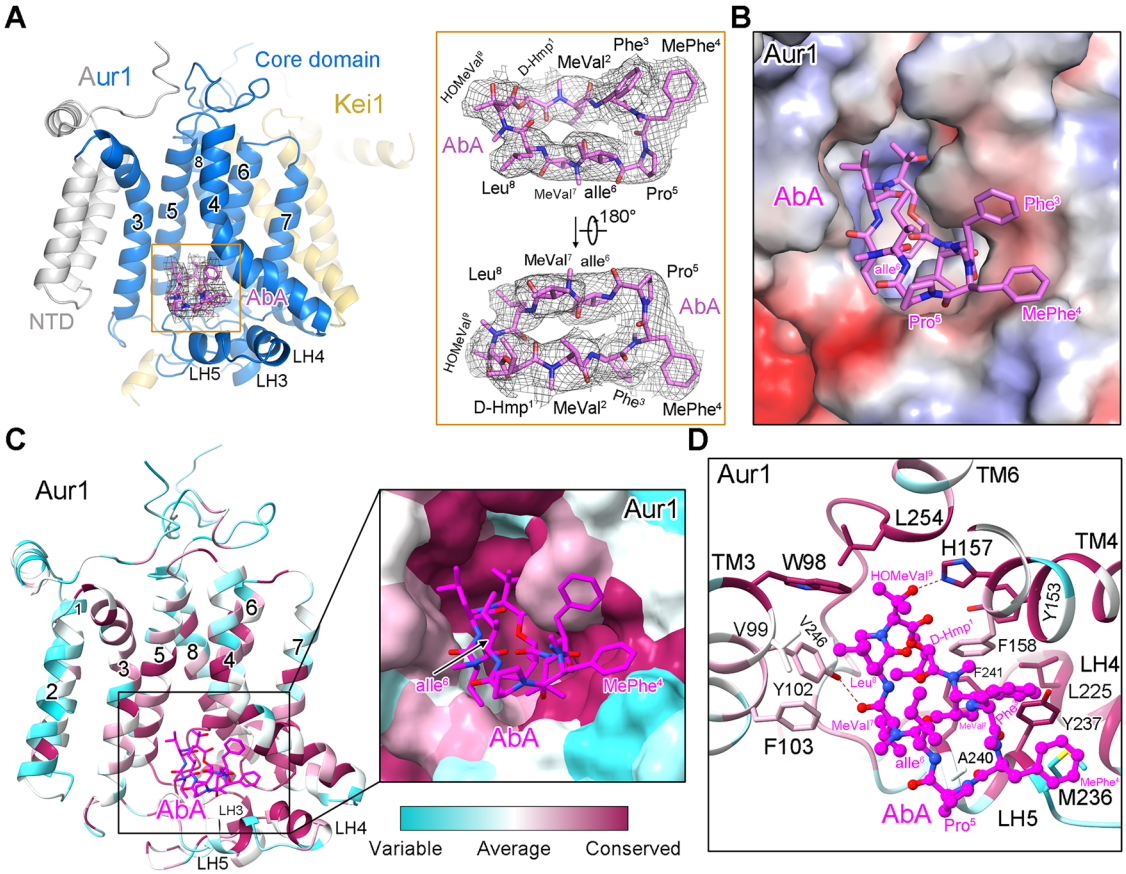

Fig. 4 | AbA binding site. A Close-up view of the AbA density within the Aur1 subunit. The EM density of AbA is displayed as a black mesh contoured at 5σ. **B** AbA is situated within a predominantly hydrophobic pocket of Aur1. **C** The AbA binding pocket is highly conserved across fungi. Aur1 is colored according to amino acid conservation scores, calculated based on the fungal Aur1 sequence alignment presented in Fig. S8. **D** Close-up view of the AbA binding interface. Aur1 is colored based on conservation scores, with AbA-interacting residues shown as sticks. Potential polar interactions are indicated by dashed lines.

binding pocket uncovered in this study denotes a hotspot for the evolution of AbA resistance in fungi.

To validate the AbA-resistance mechanism associated with these mutations, we introduced the L137F/H157Y, F158Y, and A240C mutations into the *Sc*Aur1-Kei1 complex. Additionally, we generated two single-point mutations, L137F and H157Y, to assess the functional contribution of each mutation individually. All mutant complexes were successfully purified to homogeneity, similar to the WT complex, indicating that these mutations did not disrupt complex assembly (Fig. S11A). Microscale thermophoresis (MST) measurements, a widely used method for quantifying biomolecular interactions[54], revealed that the binding affinity (K_d) between AbA and the WT Aur1-Kei1 complex is approximately 57.7 nM (Fig. 6B). However, the interaction between AbA and the L137F/H157Y mutant complex was nearly undetectable, while the F158Y and A240C mutations weakened the binding affinity by 1.5- to 2-fold (Fig. 6B). The H157Y single-point mutation resulted in a nearly 30-fold reduction in AbA binding affinity, whereas the L137F single-point mutation had little effect (Fig. 6B). This indicates that the H157Y mutation, rather than L137F, is primarily responsible for the evolution of AbA resistance in the L137F/H157Y mutant fungi. Consistent with these binding affinity data, the purified L137F/H157Y and H157Y mutants showed minimal inhibition by AbA, and the AbA-mediated inhibition of the F158Y and A240C mutants was also reduced (Figs. 6C and S11B).

Given the overlap between the potential substrate-binding pockets and the AbA-binding pocket, we sought to assess whether AbA-resistant mutations alter the affinity for the PI substrate by determining the K_m values of the mutant complexes, including H157Y, F158Y, and A240C. The results indicated that these mutations had a minor impact on the apparent affinity of IPC synthase for the PI substrate (Fig. S11C). Consistent with this, a previous study demonstrated that the F158Y mutation in Aur1 does not essentially alter the affinities for either substrate[42]. Collectively, these findings suggest that the mechanism underlying AbA resistance involves a direct disruption of AbA binding, with minimal effects on substrate affinities.

Discussion

Given the widespread prevalence of fungal infections, the limited options for antifungal drugs, and the rapid evolution of drug-resistant fungi, there is an urgent need to identify novel therapeutic targets and develop new antifungal medications. IPC synthase, an essential enzyme for fungal survival and virulence, represents a promising target for the prevention and treatment of fungal infections. In this study, we determined the first cryo-EM structure of a fungal IPC synthase complex, which consists of catalytic subunit Aur1 and regulatory subunit Kei1. Structural and biochemical analyses revealed that the potent inhibitor of IPC synthase, AbA, inhibits enzyme activity by binding near the substrate-binding pockets, thereby blocking substrate entry. Mutations conferring resistance to AbA are clustered around the AbA-binding pocket, indicating that direct disruption of AbA binding underlies the mechanism of resistance. The AbA-binding pocket resolved in this study could greatly accelerate the development and optimization of antifungal therapeutics targeting fungal IPC synthase.

As we were unable to obtain the structure of apo Aur1-Kei1 complex, we compared the AbA-bound Aur1 structure with the AlphaFold-predicted apo Aur1 structure ($Aur1^{AF}$). The overall fold of apo $Aur1^{AF}$ agrees well with our experimental model, with an overall Cα root-

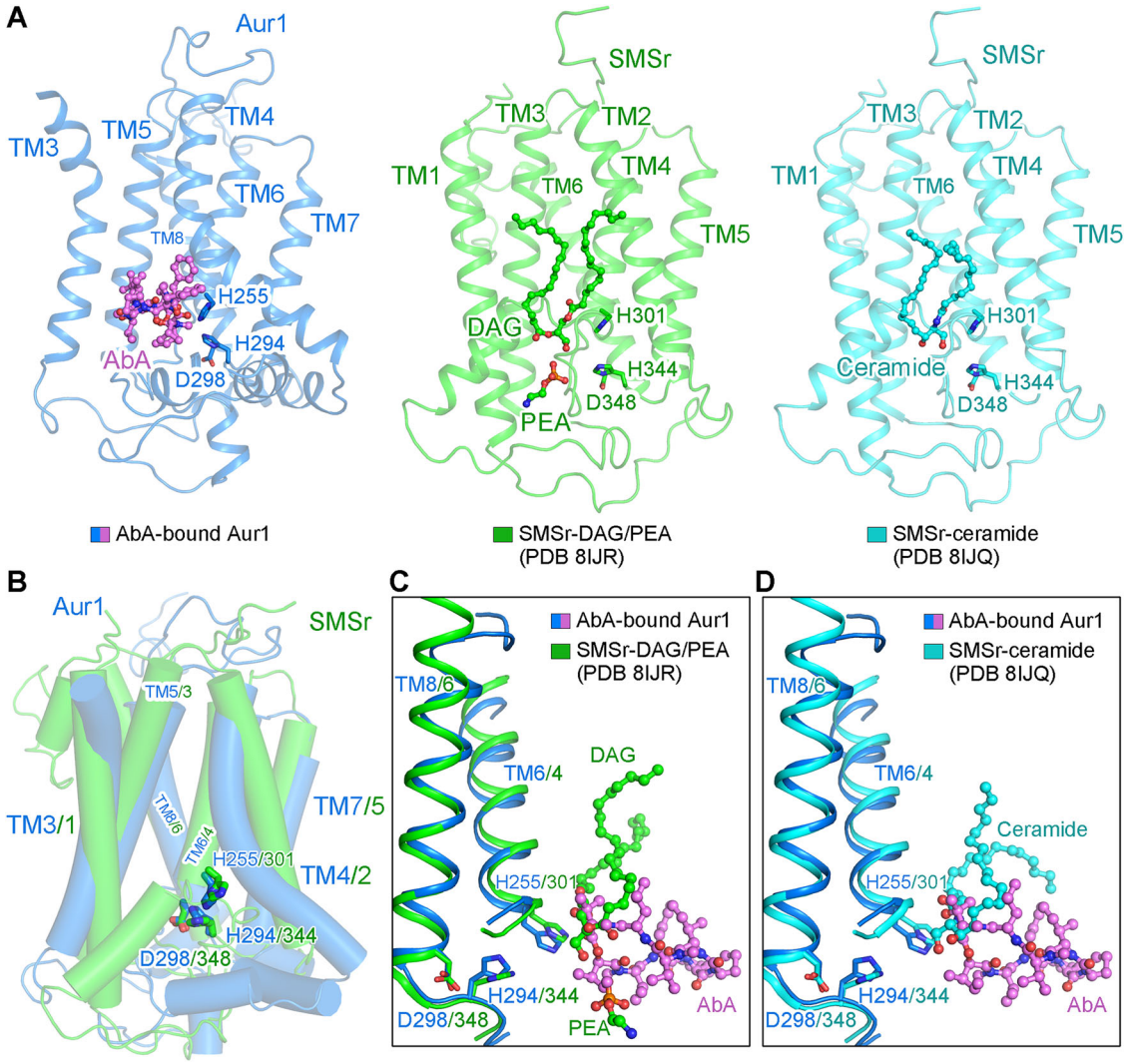

Fig. 5 | AbA blocks the entry of both substrates. A Structures of the AbA-bound Aur1, DAG/PEA-bound SMSr, and ceramide-bound SMSr. The catalytic triad residues of Aur1 and SMSr are highlighted as sticks. **B** The SMSr structure aligns well with TM3-TM8 of the catalytic core domain of Aur1, with the catalytic triads positioned identically. **C, D** Structural superposition of the AbA-bound Aur1 structure with the DAG/PEA-bound SMSr (**C**) and ceramide-bound SMSr (**D**) structures suggests that AbA blocks the entry of both substrates.

mean-square deviation (RMSD) of 1.05 Å (Fig. S12A). The catalytic triad residues (His255, His294, Asp298) are positioned identically in both structural models (Fig. S12B), and similar substrate-binding pockets are observed in both structures (Fig. S12C). These findings suggest that while AbA stabilizes the Aur1-Kei1 complex for structural determination, it does not induce significant conformational changes in the overall structure or catalytic center. This implies that the AbA-stabilized Aur1 conformation resolved in this study likely represents a catalytically relevant state.

Despite the high similarity between our AbA-bound Aur1 structure and the AlphaFold-predicted apo Aur1 structure, a notable deviation is observed in the LH5 region of Aur1. The LH5 region of the $Aur1^{AF}$ model exhibits an approximately 3.5 Å inward movement toward the AbA-binding pocket compared to the resolved cryo-EM structure (Fig. S12D). This movement leads to a steric clash between the LH5 of $Aur1^{AF}$ and AbA (Fig. S12D), indicating a structural state incompatible with AbA binding. It remains unclear whether the Aur1 conformation observed in this study is induced by AbA binding, which would require validation through experimental determination of the apo Aur1-Kei1 complex structure. Nonetheless, given the widespread use of AlphaFold for structure prediction and artificial intelligence (AI)-facilitated drug development, this analysis highlights the need for caution when using AlphaFold-predicted structures for small-molecule docking. The accuracy of these predicted models may not always be reliable, and small molecules can induce conformational changes in proteins.

In addition to AbA, several other compounds, such as khafrefungin, rustmicin, and pleofungins, have been identified as effective inhibitors of fungal IPC synthase[55–57]. Khafrefungin is a modified alkyl chain esterified aldonic acid, rustmicin is a 14-membered macrolide, and pleofungins are novel depsipeptides. These compounds possess distinct structures compared to AbA, suggesting they may inhibit IPC synthase through different mechanisms. Further research into the inhibitory mechanisms of these compounds could facilitate the development of a diverse range of IPC synthase inhibitors for the treatment of fungal infections. Overall, the findings presented in this study significantly advance our understanding of IPC synthase and could greatly aid the optimization and rational design of antifungal drugs targeting this enzyme.

Methods

Protein expression and purification

The cDNA of Aur1 and Kei1 was subcloned into the pCAG vector with either a Strep or Flag tag. Primers used in this study have been listed in Table S2. HEK293F suspension cells (Invitrogen), cultured at 37 °C with

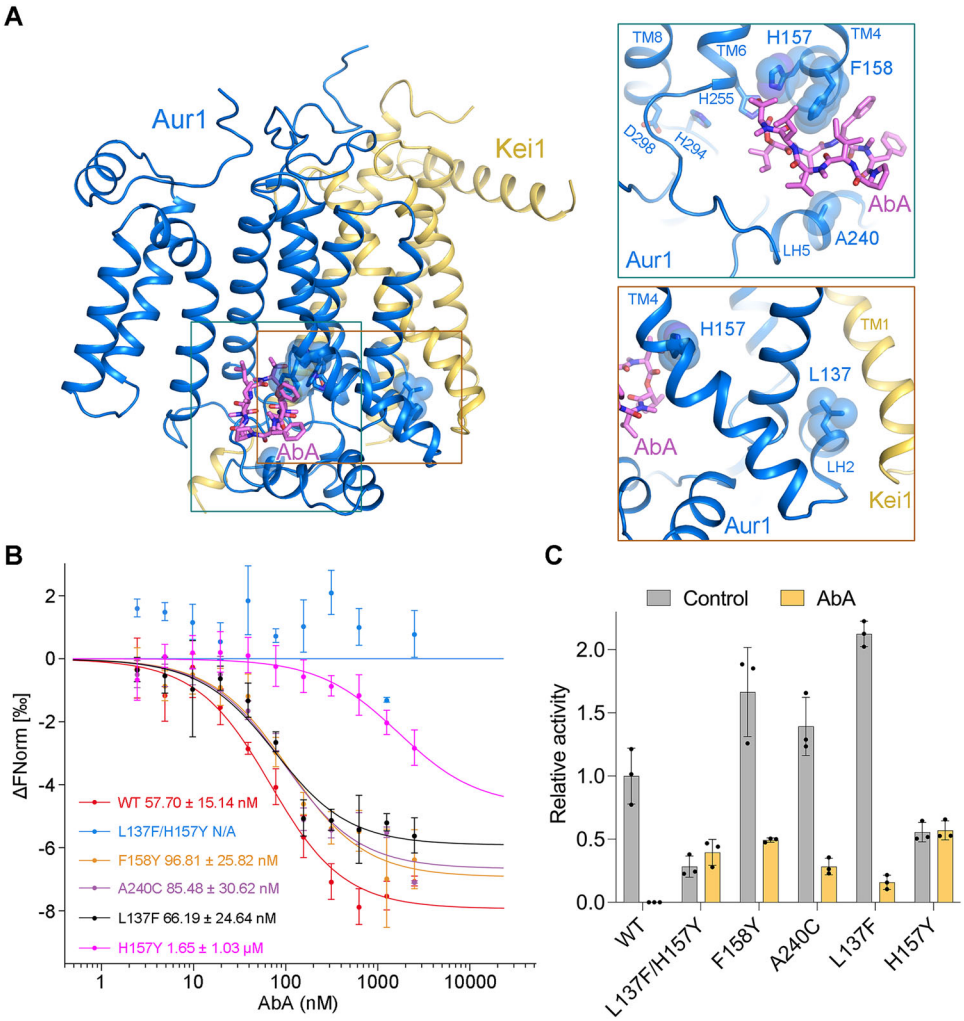

Fig. 6 | AbA resistance mechanism. A Localization of genetically identified AbA-resistant mutation sites. The AbA-resistant mutation sites are highlighted as spheres. **B** MST analysis of the binding affinities between Aur1-Kei1 variants and AbA. Each data point represents the mean ± SD of three independent measurements. **C** Normalized activity of Aur1-Kei1 variants in the absence or presence of AbA. The activities of Aur1-Kei1 variants are normalized relative to the WT Aur1-Kei1 complex in the absence of AbA. Each data point represents the mean ± SD of three independent experiments. Source data are provided as a Source Data file.

5% CO_2 in SMM 293T-II medium (Sino Biological Inc., Cat# M293TII), were used for recombinant protein expression. For protein overexpression, a total of 1.8 mg of plasmids were co-transfected with 5.4 mg polyethyleneimine (Yeasen, Cat# 40816ES03) per liter of cells at a density of 2.5–3.0 × 10^6/ml. For the overexpression of Aur1 or Kei1 alone, 1.8 mg of the respective plasmid was used per liter of cells. To achieve efficient overexpression of the IPC synthase complex, the ratio of plasmids encoding Aur1 and Kei1 was optimized. Ultimately, 1.8 mg of total plasmids, consisting of 0.6 mg of the Aur1 plasmid and 1.2 mg of the Kei1 plasmid, were used per liter of cells. After 12 hours of transfection, 10 mM sodium butyrate (Sigma-Aldrich, Cat# 303410) was added, and the cells were cultured for an additional 48 hours before being harvested.

The harvested cells were resuspended in a lysis buffer containing 25 mM HEPES pH 7.5 and 150 mM NaCl. For protein purification, 1% (w/v) LMNG (Anatrace, Cat# NG310) was used to extract membranes for 2 hours at 4 °C. After centrifugation at 37,000 g for 30 minutes at 4 °C, the supernatant was collected and incubated with Strep-Tactin affinity resin (IBA, Cat# 2-5010-010) or anti-Flag G1 affinity resin (GenScript, Cat# L00432) for 1 hour at 4 °C. To wash impurities from the resin, 5 mM ATP and 5 mM $MgCl_2$ were added to buffer W containing 25 mM HEPES pH 7.5, 150 mM NaCl, and 0.01% LMNG. The tagged protein was then eluted using buffer W supplemented with 50 mM biotin or 200 μg/mL Flag peptide. The eluted protein solution was concentrated and subjected to size-exclusion chromatography (SEC) using Superose 6 Increase 10/300 GL (Cytiva, Cat# 29-0915-96) or Superdex 200 Increase 10/300 GL (Cytiva, Cat# 28-9909-44) columns equilibrated in buffer W. The peak fractions were collected and concentrated for subsequent biochemical experiments or cryo-EM analysis.

Crosslinking of IPC synthase complex

Protein fractions from the SEC were collected for glutaraldehyde-mediated crosslinking analysis. IPC synthase at a concentration of 0.22 mg/mL was treated without or with glutaraldehyde (Sigma-Aldrich, Cat# G5882) at concentrations of 0.25%, 1%, or 2.5% (v/v) in 25 mM HEPES pH 7.5, 150 mM NaCl, and 0.01% LMNG. Each reaction had a total volume of 10 μL and was incubated for 90 minutes at 4 °C. The reaction was quenched with 100 mM Tris-HCl pH 7.0. The samples were then analyzed by SDS-PAGE.

In vitro IPC synthase activity assay

The in vitro activity of IPC synthase was measured using a thin-layer chromatography (TLC)-based fluorescent assay, as previously described[36,40,41]. A typical reaction mixture contained 25 mM HEPES pH 7.5, 150 mM NaCl, 0.01% LMNG, 10% DMSO, 500 μM soy PI (Avanti Polar Lipids, Cat# 840044 P), and 10 μM C6-NBD-ceramide (Avanti Polar

Lipids, Cat# 810209 P). The mixture was preincubated for 10 minutes at 30 °C. To initiate the reaction, purified protein was added at a final concentration of 50 nM, and the reaction was carried out at 30 °C. To terminate the reaction, 80 μL of chloroform-methanol (2:1, v/v) was added to 10 μL of the reaction mixture. The solution was vortexed thoroughly to ensure complete extraction and then centrifuged at 18,000 g for 10 minutes to separate the aqueous and organic phases. The lower organic phase was collected and dried under a stream of nitrogen. The dried material was dissolved in 10 μL of chloroform and loaded onto a silica TLC plate (Merck, Cat# 1.05729). The plate was developed for 20 minutes using a chloroform-methanol-water (19.5:7.5:1.2, v/v/v) solvent. The fluorescence-labelled ceramide substrate and IPC product were detected under blue light using a Tanon 6100 imager. The intensity of the C6-NBD-IPC band was quantified using ImageJ2 software to calculate the relative IPC synthase activity. A standard amount of C6-NBD-ceramide was applied to each TLC plate as a reference for quantification and comparison between different plates.

A time-course reaction, terminated at 0, 3, 5, 7.5, 10, 20, 30, 45, or 60 minutes, was performed to determine the linear range of the reaction. Based on these results, all subsequent reactions were terminated at 5 minutes to stay within the linear range. To measure the curve of IPC synthase activity against varying concentrations of PI (ranging from 10 to 1000 μM), the concentration of C6-NBD-ceramide was fixed at 10 μM. In contrast, to measure the curve of IPC synthase activity against varying concentrations of C6-NBD-ceramide (ranging from 0.5 to 20 μM), the PI concentration was fixed at 500 μM. In AbA inhibition experiments, 50 nM protein was preincubated with varying concentrations of AbA (Macklin, Cat# A937715) for 60 minutes at 4 °C before adding substrates to initiate the reaction. All statistical analyses were performed using GraphPad Prism 10. Each data point in the dot-plot graphs and curves represents the average of three independent experiments, with error bars indicating standard deviation (SD).

Microscale thermophoresis (MST)

Before MST measurements, His-tagged IPC synthase complex protein at a concentration of 40 nM was incubated with 10 nM of RED-tris-NTA 2nd Generation dye (NanoTemper Technologies, Cat# MO-L018) for 10 minutes at 4 °C for fluorescence labelling. The labelling was performed in 2× MST buffer containing 50 mM HEPES pH 7.5, 300 mM NaCl, 0.04% LMNG, and 1 mg/mL BSA. To assess the binding affinity between IPC synthase and AbA, equal volumes of labeled protein and varying concentrations of AbA were mixed. The final concentrations of AbA in the MST measurements ranged from 2.44 to 2,500 nM. The mixture was centrifuged at 18,000 g for 10 minutes at 4 °C before loading into capillaries for MST measurement. All experiments were conducted using a Monolith NT.115 Pico instrument (NanoTemper Technologies) with 30% LED excitation power and medium MST power. K_d values were calculated using MO Affinity Analysis software (NanoTemper Technologies).

Thermal shift assay

Nano differential scanning fluorimetry (nanoDSF) was used to measure protein thermal stability and determine the melting temperature (T_m). To assess the stability of the apo IPC synthase complex, 0.1 mg/mL of purified Aur1-Kei1 protein complex in a buffer containing 25 mM HEPES pH 7.5, 150 mM NaCl, and 0.01% LMNG was loaded into capillaries for thermal unfolding profile measurement using the Tycho NT.6 (NanoTemper Technologies), following the manufacturer's instructions. The Tycho instrument records intrinsic protein fluorescence at 330 nm and 350 nm (Em330 and Em350) as the temperature increases from 35 °C to 95 °C at a rate of 30 °C/min. A curve of the ratio between Em350 and Em330 (Em350/Em330) versus temperature was generated, and the T_m value was calculated from the peak of the first derivative of this ratio. To evaluate the stability of IPC synthase in the presence of substrate or inhibitor, the protein was incubated for 1 hour at 4 °C with a final concentration of 10 μM PI, 10 μM C6-ceramide, or 5 μM AbA in 5% DMSO before nanoDSF measurement. The T_m values were determined in the same manner. All T_m values presented in the study represent the averages of three independent measurements.

Sample preparation and cryo-EM data collection

Before sample preparation, Quantifoil holey carbon R1.2/1.3 300 mesh copper grids were glow-discharged at 15 mA for 45 seconds using a PELCO easiGlow device. For the preparation of the apo IPC synthase cryo-EM sample, 3 μl of Aur1-Kei1 protein at a concentration of 9 mg/ml was applied to the glow-discharged grids. For the AbA-bound IPC synthase cryo-EM sample, the Aur1-Kei1 protein at 9 mg/mL was pre-incubated with 0.5 mM AbA at 4 °C for 30 minutes before being applied to the grids. The grids were then blotted with a blot force of 20 for 4.5 s at 8 °C with 100% humidity using a Vitrobot (Mark IV, Thermo Fisher Scientific). After blotting, the grids were plunged into liquid ethane and rapidly frozen.

For data collection, the grids were loaded onto a 300 kV Titan Krios microscope equipped with a K3 Summit direct electron detector (Gatan). The detector featured a GIF Quantum energy filter (Gatan) with a slit width of 20 eV. Both the apo and AbA-bound datasets were collected automatically using EPU software. Micrographs were captured at a nominal magnification of ×81,000 in super-resolution mode. The defocus value ranges between −2.0 and −1.0 μm. Each movie stack was exposed for 2.3 seconds and divided into 32 frames, with a total electron dose of 50 $e^-/Å^2$.

Cryo-EM data processing

For the AbA-bound Aur1-Kei1 complex, 2,310 micrographs were collected and motion-corrected using MotionCor2[58] with dose weighting. The defocus value of each micrograph was estimated with Gctf[59]. A total of 3,263,084 particles were automatically picked and extracted in Relion 3.0[60]. All subsequent data processing was performed in CryoSPARC[61]. After 2D classification, 573,599 particles were selected for multiclass ab initio reconstruction. Two rounds of heterogeneous refinement, non-uniform refinement, and local refinement yielded a final 3D reconstruction map with an overall resolution of 3.17 Å with C2 symmetry. The resolution was determined based on the gold-standard Fourier shell correlation 0.143 criterion[62] with high-resolution noise substitution[63]. For the apo Aur1-Kei1 complex dataset, 1602 micrographs were collected, with particle picking and 2D classification performed similarly to the AbA-bound complex dataset.

Model building and refinement

The AlphaFold-predicted Aur1 and Kei1 models[43] were used as initial templates for model building. Both models were docked into the AbA-bound Aur1-Kei1 map using UCSF Chimera[64]. Manual adjustments to each residue were made in Coot[65]. The modified model was then refined in real space using Phenix, with secondary structure and geometry restraints applied[66]. Model validation was performed using Phenix and MolProbity[67]. A summary of the refinement and validation statistics is provided in Table S1. All structural figures were prepared with PyMol[68] or Chimera.

Reporting summary

Further information on research design is available in the Nature Portfolio Reporting Summary linked to this article.

Data availability

The cryo-EM density map of the AbA-bound Aur1-Kei1 complex generated in this study has been deposited in the Electron Microscopy Data Bank (EMDB) under accession code EMD-60924. The atomic model of the AbA-bound Aur1-Kei1 complex generated in this study has been deposited in the Protein Data Bank (PDB) under accession code 9IVC. Source data are provided with this paper.

References

1. Brown, G. D. et al. The pathobiology of human fungal infections. *Nat. Rev. Microbiol.* https://doi.org/10.1038/s41579-024-01062-w (2024).
2. Rokas, A. Evolution of the human pathogenic lifestyle in fungi. *Nat. Microbiol* **7**, 607–619 (2022).
3. Bongomin, F., Gago, S., Oladele, R. O. & Denning, D. W. Global and Multi-National Prevalence of Fungal Diseases-Estimate Precision. *J Fungi (Basel)* **3**, https://doi.org/10.3390/jof3040057 (2017).
4. van Burik, J.-A. H. & Magee, P. T. Aspects of Fungal Pathogenesis in Humans. *Annu. Rev. Microbiol.* **55**, 743–772 (2001).
5. Lee, Y., Puumala, E., Robbins, N. & Cowen, L. E. Antifungal Drug Resistance: Molecular Mechanisms in *Candida albicans* and Beyond. *Chem. Rev.* **121**, 3390–3411 (2021).
6. Brown, G. D. et al. Hidden killers: human fungal infections. *Sci. Transl. Med* **4**, 165rv113 (2012).
7. Stop neglecting fungi. *Nat. Microbiol.* **2**, 17120, https://doi.org/10.1038/nmicrobiol.2017.120 (2017).
8. in *One Health: Fungal Pathogens of Humans, Animals, and Plants: Report on an American Academy of Microbiology Colloquium held in Washington, DC, on October 18, 2017 American Academy of Microbiology Colloquia Reports* (2019).
9. Ostrosky-Zeichner, L., Casadevall, A., Galgiani, J. N., Odds, F. C. & Rex, J. H. An insight into the antifungal pipeline: selected new molecules and beyond. *Nat. Rev. Drug Discov.* **9**, 719–727 (2010).
10. Perfect, J. R. The antifungal pipeline: a reality check. *Nat. Rev. Drug Discov.* **16**, 603–616 (2017).
11. Lee, Y., Robbins, N. & Cowen, L. E. Molecular mechanisms governing antifungal drug resistance. *NPJ Antimicrob. Resist* **1**, 5 (2023).
12. Lockhart, S. R., Chowdhary, A. & Gold, J. A. W. The rapid emergence of antifungal-resistant human-pathogenic fungi. *Nat. Rev. Microbiol.* **21**, 818–832 (2023).
13. Fisher, M. C. et al. Tackling the emerging threat of antifungal resistance to human health. *Nat. Rev. Microbiol.* **20**, 557–571 (2022).
14. Iyer, K. R., Revie, N. M., Fu, C., Robbins, N. & Cowen, L. E. Treatment strategies for cryptococcal infection: challenges, advances and future outlook. *Nat. Rev. Microbiol.* **19**, 454–466 (2021).
15. Berman, J. & Krysan, D. J. Drug resistance and tolerance in fungi. *Nat. Rev. Microbiol.* **18**, 319–331 (2020).
16. Fisher, M. C., Hawkins, N. J., Sanglard, D. & Gurr, S. J. Worldwide emergence of resistance to antifungal drugs challenges human health and food security. *Science* **360**, 739–742 (2018).
17. Mota Fernandes, C. & Del Poeta, M. Fungal sphingolipids: role in the regulation of virulence and potential as targets for future antifungal therapies. *Expert Rev. Anti Infect. Ther.* **18**, 1083–1092 (2020).
18. Megyeri, M., Riezman, H., Schuldiner, M. & Futerman, A. H. Making Sense of the Yeast Sphingolipid Pathway. *J. Mol. Biol.* **428**, 4765–4775 (2016).
19. Montefusco, D. J., Matmati, N. & Hannun, Y. A. The yeast sphingolipid signaling landscape. *Chem. Phys. Lipids* **177**, 26–40 (2014).
20. Rhome, R. & Del Poeta, M. Sphingolipid signaling in fungal pathogens. *Adv. Exp. Med. Biol.* **688**, 232–237 (2010).
21. Wang, J. et al. Functions of Sphingolipids in Pathogenesis During Host-Pathogen Interactions. *Front. Microbiol.* **12**, 701041 (2021).
22. Nagiec, M. M. et al. Sphingolipid synthesis as a target for antifungal drugs. Complementation of the inositol phosphorylceramide synthase defect in a mutant strain of *Saccharomyces cerevisiae* by the *AUR1* gene. *J. Biol. Chem.* **272**, 9809–9817 (1997).
23. Dickson, R. C. Sphingolipid functions in *Saccharomyces cerevisiae*: comparison to mammals. *Annu Rev. Biochem* **67**, 27–48 (1998).
24. Sugimoto, Y., Sakoh, H. & Yamada, K. IPC synthase as a useful target for antifungal drugs. *Curr. Drug Targets Infect. Disord.* **4**, 311–322 (2004).
25. Georgopapadakou, N. H. Antifungals targeted to sphingolipid synthesis: focus on inositol phosphorylceramide synthase. *Expert Opin. Investig. Drugs* **9**, 1787–1796 (2000).
26. Denny, P. W., Shams-Eldin, H., Price, H. P., Smith, D. F. & Schwarz, R. T. The protozoan inositol phosphorylceramide synthase: a novel drug target that defines a new class of sphingolipid synthase. *J. Biol. Chem.* **281**, 28200–28209 (2006).
27. Mina, J. G., Mosely, J. A., Ali, H. Z., Denny, P. W. & Steel, P. G. Exploring *Leishmania major* inositol phosphorylceramide synthase (LmjIPCS): insights into the ceramide binding domain. *Org. Biomol. Chem.* **9**, 1823–1830 (2011).
28. Dos Santos, N. S. A. et al. Disruption of the inositol phosphorylceramide synthase gene affects *Trypanosoma cruzi* differentiation and infection capacity. *PLoS Negl. Trop. Dis.* **17**, e0011646 (2023).
29. Ciganda, M., Jackson, A. P. & Bangs, J. D. Diversification of sphingolipid synthase activities in kinetoplastid protozoa. *Mol. Biochem Parasitol.* **260**, 111656 (2024).
30. Takesako, K. et al. Biological properties of aureobasidin A, a cyclic depsipeptide antifungal antibiotic. *J. Antibiot. (Tokyo)* **46**, 1414–1420 (1993).
31. Endo, M., Takesako, K., Kato, I. & Yamaguchi, H. Fungicidal action of aureobasidin A, a cyclic depsipeptide antifungal antibiotic, against *Saccharomyces cerevisiae*. *Antimicrob. Agents Chemother.* **41**, 672–676 (1997).
32. Kurome, T., Inoue, T., Takesako, K. & Kato, I. Syntheses of antifungal aureobasidin A analogs with alkyl chains for structure-activity relationship. *J. Antibiot. (Tokyo)* **51**, 359–367 (1998).
33. Wuts, P. G. et al. Generation of Broad-Spectrum Antifungal Drug Candidates from the Natural Product Compound Aureobasidin A. *ACS Med Chem. Lett.* **6**, 645–649 (2015).
34. Heidler, S. A. & Radding, J. A. The *AUR1* gene in *Saccharomyces cerevisiae* encodes dominant resistance to the antifungal agent aureobasidin A (LY295337). *Antimicrob. Agents Chemother.* **39**, 2765–2769 (1995).
35. Hashida-Okado, T. et al. *AUR1*, a novel gene conferring aureobasidin resistance on *Saccharomyces cerevisiae*: a study of defective morphologies in Aur1p-depleted cells. *Mol. Gen. Genet* **251**, 236–244 (1996).
36. Levine, T. P., Wiggins, C. A. & Munro, S. Inositol phosphorylceramide synthase is located in the Golgi apparatus of *Saccharomyces cerevisiae*. *Mol. Biol. Cell* **11**, 2267–2281 (2000).
37. Heidler, S. A. & Radding, J. A. Inositol phosphoryl transferases from human pathogenic fungi. *Biochim Biophys. Acta* **1500**, 147–152 (2000).
38. Huitema, K., van den Dikkenberg, J., Brouwers, J. F. & Holthuis, J. C. Identification of a family of animal sphingomyelin synthases. *EMBO J.* **23**, 33–44 (2004).
39. Sato, K., Noda, Y. & Yoda, K. Kei1: a novel subunit of inositolphosphorylceramide synthase, essential for its enzyme activity and Golgi localization. *Mol. Biol. Cell* **20**, 4444–4457 (2009).
40. Zhong, W., Murphy, D. J. & Georgopapadakou, N. H. Inhibition of yeast inositol phosphorylceramide synthase by aureobasidin A measured by a fluorometric assay. *FEBS Lett.* **463**, 241–244 (1999).
41. Figueiredo, J. M., Dias, W. B., Mendonca-Previato, L., Previato, J. O. & Heise, N. Characterization of the inositol phosphorylceramide synthase activity from *Trypanosoma cruzi*. *Biochem J.* **387**, 519–529 (2005).
42. Aeed, P. A., Young, C. L., Nagiec, M. M. & Elhammer, A. P. Inhibition of inositol phosphorylceramide synthase by the cyclic peptide aureobasidin A. *Antimicrob. Agents Chemother.* **53**, 496–504 (2009).
43. Jumper, J. et al. Highly accurate protein structure prediction with AlphaFold. *Nature* **596**, 583–589 (2021).
44. Evans, R. et al. Protein complex prediction with AlphaFold-Multimer. *BioRxiv*, 463034, https://doi.org/10.1101/2021.10.04.463034 %J bioRxiv (2022).
45. Lavinder, J. J., Hari, S. B., Sullivan, B. J. & Magliery, T. J. High-throughput thermal scanning: a general, rapid dye-binding thermal

shift screen for protein engineering. *J. Am. Chem. Soc.* **131**, 3794–3795 (2009).
46. Groftehauge, M. K., Hajizadeh, N. R., Swann, M. J. & Pohl, E. Protein-ligand interactions investigated by thermal shift assays (TSA) and dual polarization interferometry (DPI). *Acta Crystallogr D. Biol. Crystallogr* **71**, 36–44 (2015).
47. Nji, E., Chatzikyriakidou, Y., Landreh, M. & Drew, D. An engineered thermal-shift screen reveals specific lipid preferences of eukaryotic and prokaryotic membrane proteins. *Nat. Commun.* **9**, 4253 (2018).
48. Pantoliano, M. W. et al. High-density miniaturized thermal shift assays as a general strategy for drug discovery. *J. Biomol. Screen* **6**, 429–440 (2001).
49. Hu, K. et al. Cryo-EM structure of human sphingomyelin synthase and its mechanistic implications for sphingomyelin synthesis. *Nat. Struct. Mol. Biol.* **31**, 884–895 (2024).
50. Eberhardt, J., Santos-Martins, D., Tillack, A. F. & Forli, S. AutoDock Vina 1.2.0: New Docking Methods, Expanded Force Field, and Python Bindings. *J. Chem. Inf. Model* **61**, 3891–3898 (2021).
51. Trott, O. & Olson, A. J. AutoDock Vina: improving the speed and accuracy of docking with a new scoring function, efficient optimization, and multithreading. *J. Comput Chem.* **31**, 455–461 (2010).
52. Hashida-Okado, T., Yasumoto, R., Endo, M., Takesako, K. & Kato, I. Isolation and characterization of the aureobasidin A-resistant gene, *aur1R*, on *Schizosaccharomyces pombe*: roles of *Aur1p+* in cell morphogenesis. *Curr. Genet* **33**, 38–45 (1998).
53. Kuroda, M. et al. An aureobasidin A resistance gene isolated from *Aspergillus* is a homolog of yeast *AUR1*, a gene responsible for inositol phosphorylceramide (IPC) synthase activity. *Mol. Gen. Genet* **261**, 290–296 (1999).
54. Jerabek-Willemsen, M. et al. MicroScale Thermophoresis: Interaction analysis and beyond. *J. Mol. Struct.* **1077**, 101–113 (2014).
55. Mandala, S. M. et al. Khafrefungin, a novel inhibitor of sphingolipid synthesis. *J. Biol. Chem.* **272**, 32709–32714 (1997).
56. Mandala, S. M. et al. Rustmicin, a potent antifungal agent, inhibits sphingolipid synthesis at inositol phosphoceramide synthase. *J. Biol. Chem.* **273**, 14942–14949 (1998).
57. Yano, T. et al. Pleofungins, novel inositol phosphorylceramide synthase inhibitors, from *Phoma* sp. SANK 13899. I. Taxonomy, fermentation, isolation, and biological activities. *J. Antibiot. (Tokyo)* **60**, 136–142 (2007).
58. Zheng, S. Q. et al. MotionCor2: anisotropic correction of beam-induced motion for improved cryo-electron microscopy. *Nat. Methods* **14**, 331–332 (2017).
59. Zhang, K. Gctf: Real-time CTF determination and correction. *J. Struct. Biol.* **193**, 1–12 (2016).
60. Zivanov, J. et al. New tools for automated high-resolution cryo-EM structure determination in RELION-3. *Elife* **7**, https://doi.org/10.7554/eLife.42166 (2018).
61. Punjani, A., Rubinstein, J. L., Fleet, D. J. & Brubaker, M. A. cryoSPARC: algorithms for rapid unsupervised cryo-EM structure determination. *Nat. Methods* **14**, 290–296 (2017).
62. Rosenthal, P. B. & Henderson, R. Optimal determination of particle orientation, absolute hand, and contrast loss in single-particle electron cryomicroscopy. *J. Mol. Biol.* **333**, 721–745 (2003).
63. Chen, S. X. et al. High-resolution noise substitution to measure overfitting and validate resolution in 3D structure determination by single particle electron cryomicroscopy. *Ultramicroscopy* **135**, 24–35 (2013).
64. Pettersen, E. F. et al. UCSF Chimera-a visualization system for exploratory research and analysis. *J. Comput Chem.* **25**, 1605–1612 (2004).
65. Emsley, P., Lohkamp, B., Scott, W. G. & Cowtan, K. Features and development of Coot. *Acta Crystallogr D. Biol. Crystallogr* **66**, 486–501 (2010).
66. Adams, P. D. et al. PHENIX: a comprehensive Python-based system for macromolecular structure solution. *Acta Crystallogr D.* **66**, 213–221 (2010).
67. Williams, C. J. et al. MolProbity: More and better reference data for improved all-atom structure validation. *Protein Sci.* **27**, 293–315 (2018).
68. DeLano, W. L. The PyMOL Molecular Graphics System on World Wide Web http://www.pymol.org. (2002).

Acknowledgements

We thank the Cryo-EM Facility of the Southern University of Science and Technology (SUSTech) for providing the facility support. This work was supported by the National Natural Science Foundation of China (Grant No. 32401001 to T.X.), and the Shenzhen Science and Technology Program (Grant No. JCYJ20240813094404006 to T.X.; Grant No. KQTD20190929173906742; and Grant No. ZDSYS20230626091659010). X.G. is an investigator of SUSTech Institute for Biological Electron Microscopy.

Author contributions

X.G. conceived and supervised the project. X.G., T.X., and X.W. designed the experiments. T.X. and X.W. conducted the experiments. All authors contributed to the data analysis. T.X. and X.G. wrote the manuscript.

Competing interests

The authors declare no competing interests.

Additional information

Supplementary information The online version contains supplementary material available at https://doi.org/10.1038/s41467-025-60423-y.

Correspondence and requests for materials should be addressed to Xin Gong or Tian Xie.

Peer review information *Nature Communications* thanks the anonymous reviewers for their contribution to the peer review of this work. A peer review file is available.